Signal Detection for Underwater IoT Devices with Long and Sparse Channels

Shusen Jing, *Student Member, IEEE,* Joseph Hall, Yahong Rosa Zheng, *Fellow, IEEE,*
and Chengshan Xiao, *Fellow, IEEE*

(Invited Paper)

***Abstract*—Underwater acoustic communication often suffers from extended channel impulse response and large Doppler spread, such that signals become difficult to detect and decode. For underwater internet of things (IoT) applications, the challenges are even bigger, because IoT devices usually transmit very short messages due to severe power constraints, and the length of pilots are often shorter than that of channel impulse response. Therefore, conventional pilot-assisted channel estimation and equalization approaches are incapable of detecting information data. Moreover, existing blind channel equalization algorithms, which do not require pilots, are not able to detect information data either, because the number of transmitted symbols is too small to approximate the expected loss with empirical loss, where the loss refers to as the error of estimated signal envelopes. In this paper, a new equalization and decoding algorithm is proposed for underwater IoT devices under harsh communication environments. Inspired by recent blind deconvolution and compressive sensing techniques, we construct an optimization problem with objective function rewarding sparsity of the estimated channel impulse response using l_4-norm, and convexify the feasible set of the problem while guarantee the same solution. Then we develop a pruned tree search initialization method, and use gradient descent to find an optimal solution efficiently. The new algorithm is first verified by simulations, which show that the proposed algorithm outperforms conventional methods such as linear minimum mean square error (LMMSE) equalizer and constant modulus algorithm (CMA). The proposed algorithm, along with a practical procedure for compensating large Doppler spread and carrier frequency offset, is further employed to process real-world underwater IoT data collected in a fish-tag project. It shows that the proposed algorithm can equalize and detect IoT data which was corrupted by channels whose length are longer than that of pilots, but existing algorithms such as LMMSE equalizer and CMA-based blind equalizer are not able to accomplish. It also shows that the proposed algorithm can provide a very impressive improvement compared to raw detection (no equalization or decoding) and decoding-only approaches.**

***Index Terms*—Underwater acoustic communication, sparse multipath channel, channel equalization, IoT devices.**

I. INTRODUCTION

THE idea of internet of things (IoT) first began in 1982 when researchers used some small devices to report basic information of daily products. The system only involved simple sensors reporting the collected data. Then in 1999, the phrase IoT was first time invented as increasing data had been created by devices instead of human. As the communication technologies developed and embedded system designs become more sophisticated, it becomes possible to connect different self-control devices to internet. In 2003 the things-to-people ratio was only 0.08, while that increased to 1.84 in 2010 [1]. Today IoT draw much attention of people and a large number of IoT systems have been implemented for different purposes. The advantages of IoT system are remarkable. Small devices can be implemented in different places to monitor, collect and send data, which is sometimes impossible for human to do [2]. For example, it can measure the temperature of water and send results back to human automatically without a break, while this task can cost expensive human resources.

Today's IoT systems are supported by novel communication technologies [3, 4], hardware design strategies, and big data processing, however problems arose in IoT systems are still challenging. Many IoT devices need to work in very harsh environments, and implementing devices in such environments is expensive for even one-time effort. Therefore people want the devices to work as long time as possible before next maintenance or being discarded. For the purpose to save power, many devices are designed to transmit very short messages, but such designs can arise problems at receiver in communication systems.

Oceans take up most of the earth surface while many mysteries remain unknown to people. Researchers make lots of efforts in studying oceans, and one of the tasks is to understand more about marine animals. In order to do that, people put IoT devices into animals' bodies to collect data related to their movements and quantities [5]. These small devices transmit identity messages of animals regularly through water, and people collect these messages for analysis. Such underwater acoustic communication systems [6] can suffer from severe multipath channels, Doppler spread, interference and noise.

When short IoT signals meet severe multipath channels, conventional channel estimation and equalization methods, such as zero-forcing (ZF) and linear minimum mean square error (LMMSE), cannot work. Since pilots in such signals

Manuscript received November 30, 2019; revised February 22, 2020; accepted March 17, 2020. Date of publication March 31, 2020; date of current version August 12, 2020. *(Corresponding author: Chengshan Xiao.)*

The authors are with the Department of Electrical and Computer Engineering, Lehigh University, Bethlehem, 18015, USA (e-mail: shj218@lehigh.edu, jwh318@lehigh.edu, yrz218@lehigh.edu and xiaoc@lehigh.edu).

Digital Object Identifier 10.1109/JIOT.2020.2984532

are shorter than channel impulse response (CIR), the number of linear equations related to pilots is smaller than the number of unknown taps, which makes linear equation systems for channel estimation underdetermined. Blind equalization refers to equalizing channel without knowing CIR. One of most common methods is constant modulus algorithm (CMA) [7, 8], which adjusts linear equalizer coefficients to minimize expectation error of envelopes of received signal. However, it cannot be used in short signal scenarios, since CMA tries to minimize expected error of estimated signal envelopes while short signals do not contain enough symbols to make emprical error close to expected error. The problem encountered here is a special tpye of blind deconvolution (BD), which deconvolves two unknown signals with their convolution results [9–11]. [9] solves the subspace-constrained BD by minimizing nuclear norm of 'lifted' matrix with linear constraints, which is a convex programming. However, this cannot be adopted to solve our problem, because it requires the number of constraints to be much larger than the number of unknown variables, which cannot be achieved in our cases. [10, 11] solve and analyize sparse constrained BD via non-convex programmings on sphere. Even though [10, 11] consider sparsity, which is a key property of CIR, their methods still cannot be directly adopted, since constraints in our problem, such as linear convolutions and pilots, will harm the symmetry of the objective geometries on sphere, which results in degraded performance.

To address short message equalization and decoding problems, we first prove that these problems are identifiable if they satisfy three conditions. Then a non-convex optimization problem is constructed, by solving which we can obtain the equalization detection results. In order to obtain an optimal solution in the non-convex optimization, a pruned tree search initialization algorithm is proposed. With good initialization, our proposed optimization methods show significant advantages over other algorithms. In addition, complete procedures for real-world data processing are proposed, and $28,000$ real-world underwater IoT data recordings collected by Pacific Northwest National Laboratory (PNNL) fish-tag project are used to test our algorithm. The results show that our methods significantly improve successful detection rate.

The rest of the paper is organized as follows. System model and conventional equalization techniques are reviewed in Section II. Main algorithms and simulation results are illustrated in Section III. Section IV shows the data processing procedures and experimental results. Section V finally concludes the paper.

II. SYSTEM MODEL AND PRELIMINARIES

Consider a block of bits $\mathbf{v}_d \in \mathbb{B}^{M_{d1}\times 1}$ going to be transmitted. It is first encoded by a forward error correction code resulting in $\mathbf{u}_d = [\mathbf{v}_d; \mathbf{c}_d] \in \mathbb{B}^{M_d\times 1}$, where $\mathbf{c}_d \in \mathbb{B}^{M_{d2}\times 1}$ are parity check bits, and $M_d = M_{d1} + M_{d2}$. Then pilot bits $\mathbf{u}_p \in \mathbb{B}^{M_p\times 1}$ are prepended to give $\mathbf{u} = [\mathbf{u}_p; \mathbf{u}_d] \in \mathbb{B}^{M\times 1}$, where $M = M_p + M_d$. After that, $\mathbf{u}$ is mapped to $\mathbf{x} = [\mathbf{x}_p; \mathbf{x}_d] \in \{-1, 1\}^{M\times 1}$ via binary phase shift keying (BPSK) modulation. Through a pulse shaping filter, baseband signal can be expressed as

$$b(t) = \sum_{i=1}^{M} x(i)p(t-(i-1)T_b) \tag{1}$$

where T_b denotes BPSK symbol duration and $p(t)$ is pulse shaping. Then $b(t)$ is modulated with carrier frequency f_c and transmitted through a multipath channel. At receiver end, coherent demodulation is applied and results in baseband received signal

$$\tilde{r}(t) = [b(t)e^{j(2\pi\Delta f t-\theta)}] * \tilde{h}(t) + \tilde{n}(t) \tag{2}$$

where $\tilde{h}(t) \in \mathbb{C}$ is equivalent baseband CIR, $n(t)$ is additive Gaussian noise. Δf refers to frequency shift error including carrier frequency offset (CFO) and Doppler shift, and θ is the initial phase. '$*$' refers to linear convolution operation. With Δf and θ being estimated accurately, we have the received baseband signal

$$r(t) = b(t) * \breve{h}(t) + n(t) \tag{3}$$

where $r(t) = \tilde{r}(t)e^{-j(2\pi\Delta f t-\theta)}$, and $\breve{h}(t) = \tilde{h}(t)e^{-j2\pi\Delta f t}$. Downsample $r(t)$ with sampling interval T_b, we have eq. (3) written in discrete-time symbol-spaced input-output relation:

$$y(k) = \sum_{l=1}^{L} h(l)x(k-l+1) + n(k) \tag{4}$$

where $\{h(l)\}_{l=1}^{L}$ are the baseband CIR with sampling interval T_b [1], $\{y(k)\}_{k=1}^{N}$, where $N = M + L - 1$, are the received symbols, and $\{n(k)\}_{k=1}^{N}$ are the additive white Gaussian noise with zero mean and variance σ^2.

Since short signals are considered, we assume $x(k) = 0$ if $k < 1$ or $k > M$. We further assume that $h(k) = 0$ if $k < 1$ or $k > L$. Denote $\mathbf{y} = [y(1), y(2), ..., y(N)]^T$, $\mathbf{h} = [h(1), h(2), ..., h(L)]^T$ and $\mathbf{n} = [n(1), n(2), ..., n(N)]^T$, then eq. (4) can be rewritten as

$$\mathbf{y} = \mathbf{C_x h} + \mathbf{n} = \mathbf{C_h x} + \mathbf{n} \tag{5}$$

where $\mathbf{C_x}(i,j) = x(i-j+1)$ and $\mathbf{C_h}(i,j) = h(i-j+1)$. In baseband processing at receiver end, channel equalizer and decoder are used to recover $\mathbf{v}_d$ (or $\mathbf{x}$), given $\mathbf{y}$ and $\mathbf{x}_p$. The above system model is depicted in Fig. 1.

For conventional coherent receiver, channel estimation is required before equalization, detection and decoding. Denote $\mathbf{y}_k = [y(1), y(2), ..., y(k)]^T$, $\mathbf{h}_k = [h(1), h(2), ..., h(k)]^T$, $\mathbf{n}_k = [n(1), n(2), ..., n(k)]^T$, and $\mathbf{C}_{\mathbf{x},M_p}$ as the first M_p rows of $\mathbf{C_x}$. Then the first M_p rows of eq. (5) can be expressed as

$$\mathbf{y}_{M_p} = \mathbf{C}_{\mathbf{x},M_p}\mathbf{h} + \mathbf{n}_{M_p}. \tag{6}$$

With LMMSE channel estimation, the estimated channel can be expressed as

$$\hat{\mathbf{h}} = (\mathbf{C}_{\mathbf{x},M_p}^H \mathbf{C}_{\mathbf{x},M_p} + \sigma^2\mathbf{I})^{-1}\mathbf{C}_{\mathbf{x},M_p}^H \mathbf{y}_{M_p} \tag{7}$$

---

[1] $\{h(l)\}_{l=1}^{L}$ are obtained by downsampling $\breve{h}(t) * p(t)$ instead of $\breve{h}(t)$.

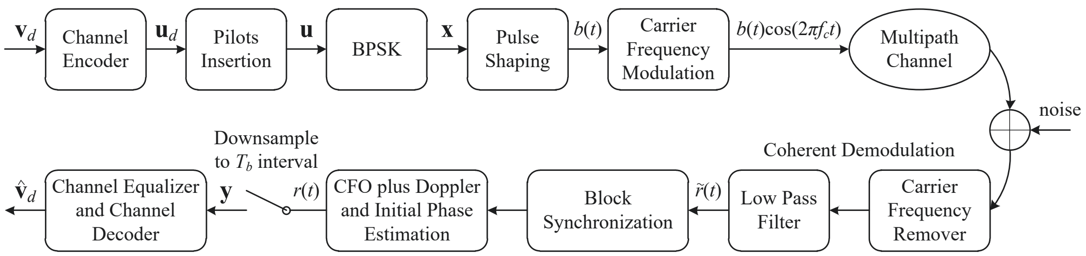

Fig. 1. System model for IoT transceiver.

where $\mathbf{I}$ refers to as identity matrix. Denote the first M_p columns of $\mathbf{C}_{\hat{\mathbf{h}}}$ as $\mathbf{C}_{\hat{\mathbf{h}},p}$ and the rest as $\mathbf{C}_{\hat{\mathbf{h}},d}$, then LMMSE equalizer gives

$$\hat{\mathbf{x}}_d = (\mathbf{C}_{\hat{\mathbf{h}},d}^H \mathbf{C}_{\hat{\mathbf{h}},d} + \sigma^2 \mathbf{I})^{-1} \mathbf{C}_{\hat{\mathbf{h}},d}^H (\mathbf{y} - \mathbf{C}_{\hat{\mathbf{h}},p} \mathbf{x}_p). \tag{8}$$

Here eq. (8) is based on the assumption that channel estimation is accurate with the number of pilots $M_p \geq 2L - 1$. However, things are significantly different when $M_p < L$, for which the linear problem described in eq. (6) becomes ill-conditioned with the number of unknowns L being larger than the number of independent linear equations M_p. To this end, different channel estimation and equalization strategies are necessary.

III. PROPOSED EQUALIZATION AND DECODING

Blind equalization is well studied over decades. Many algorithms including constant modulus (CM) and other adaptive filter based algorithms can perform well for long messages. However, one key difference between the scenarios of this paper and others is that the length of transmitted signals are short in this paper. This means that we do not have long received signals to help us infer the CIR. Another difference is that we have a small number of pilots which is not enough to estimate channels properly. Besides, in underwater acoustic communication, CIRs are usually sparse. Adopting ideas from compressive sensing, the *a priori* information of sparse channels helps us construct problems effectively.

A. Identifiability

Blind equalization is a special type of blind deconvolution. Most blind (circular) deconvolution problems are not identifiable, and they can only be recovered up to a scaled and signed shift version of the ground truth. For our specific problem, we have the following proposition to guarantee the identifiability.

Proposition 1. *The problem is identifiable with probability approaching to* 1*, if the following conditions hold: (1) There is no noise; (2) There is at least one pilot; and (3) The probability measure function* $\mathrm{p}(\mathbf{h} \in E) = 0$ *if* $\mathcal{M}(E) = 0$*, where* $\mathcal{M}$ *is Lebesgue measure.*

Proof. Without loss of generality, we assume $x(1) = 1$ is known. Suppose ambiguity exists, then there exist $\mathbf{C}_{\mathbf{x_1}}$, $\mathbf{C}_{\mathbf{x_2}}$ and $\mathbf{h_1}$, $\mathbf{h_2}$ such that

$$\mathbf{y} = \mathbf{C}_{\mathbf{x_1}} \mathbf{h_1} = \mathbf{C}_{\mathbf{x_2}} \mathbf{h_2}. \tag{9}$$

This means $\mathbf{y} \in range(\mathbf{C}_{\mathbf{x_1}}) \cap range(\mathbf{C}_{\mathbf{x_2}})$. Denote the basis of $range(\mathbf{C}_{\mathbf{x_1}}) \cap range(\mathbf{C}_{\mathbf{x_2}})$ as $\mathbf{V} = \mathbf{C}_{\mathbf{x_1}}\mathbf{T}$. Then all possible $\mathbf{h_1}$ making ambiguity are in $range(\mathbf{T})$.

Note that $rank(\mathbf{T}) \leq L$. If $rank(\mathbf{T}) < L$, then $\mathrm{p}(\mathbf{h_1} \in range(\mathbf{T})) = 0$ by the third condition, since $\mathcal{M}(range(\mathbf{T})) = 0$. If $rank(\mathbf{T}) = L$, then $range(\mathbf{C}_{\mathbf{x_1}}) = range(\mathbf{C}_{\mathbf{x_2}})$. This means every vector in $\mathbf{C}_{\mathbf{x_2}}$ can be written as linear combination of vectors in $\mathbf{C}_{\mathbf{x_1}}$. Consider the first column of $\mathbf{C}_{\mathbf{x_2}}$, there exists a vector $\mathbf{q}$ such that

$$\mathbf{C}_{\mathbf{x_2}}(:,1) = \mathbf{C}_{\mathbf{x_1}}\mathbf{q}. \tag{10}$$

Note that the indexes of non-zero entries in $\mathbf{C}_{\mathbf{x_2}}(:,1)$ are $\{1, 2, ..., M\}$. If $q(N) \neq 0$ then the N-th entry of $\mathbf{C}_{\mathbf{x_1}}\mathbf{q}$ is non-zero, which contradicts to the fact that $\mathbf{C}_{\mathbf{x_2}}(:,1)$ has 0 at the N-th entry. Therefore $q(N) = 0$. Then if $q(N-1) \neq 0$, since we have $q(N) = 0$, it will contradict to the fact that $\mathbf{C}_{\mathbf{x_2}}(:,1)$ has 0 at the $(N-1)$-th entry. Similarly, we can infer that $\forall i > 1, q(i) = 0$, and

$$\mathbf{C}_{\mathbf{x_2}}(:,1) = q(1)\mathbf{C}_{\mathbf{x_1}}(:,1). \tag{11}$$

Since we have pilot $x_1(1) = x_2(1) = 1$, the first columns of $\mathbf{C}_{\mathbf{x_1}}$ and $\mathbf{C}_{\mathbf{x_2}}$ have to be same. Apply similar approach to other columns of $\mathbf{C}_{\mathbf{x_1}}$ and $\mathbf{C}_{\mathbf{x_2}}$, we finally conclude $\mathbf{C}_{\mathbf{x_1}} = \mathbf{C}_{\mathbf{x_2}}$.

$\square$

Apparently, many common types of distributions follow the conditions in Proposition 1. However, these conditions are sufficient but may not be necessary. For example, though we generate entries of $\mathbf{h}$ as independent identically distributed (i.i.d.) Bernoulli-Gaussian (BG) random variables [11] in simulations, which violates the third condition, the problem can still be identifiable for most of the time.

B. Optimization Problem Construction

Let matrix $\mathbf{Y}$ denote

$$\mathbf{Y} = \begin{bmatrix} y(1) & y(2) & \dots & y(M) \\ y(2) & y(3) & \dots & y(M+1) \\ \vdots & \vdots & \ddots & \vdots \\ y(L) & y(L+1) & \dots & y(L+M-1) \end{bmatrix}. \tag{12}$$

Then we construct an optimization problem as

$$\min_{\mathbf{x}=[\mathbf{x}_p;\mathbf{x}_d]} -\frac{1}{4}||\mathbf{Y}\mathbf{x}||_{l_4}^4$$
$$s.t. \ \ \mathbf{x}_d \in \{-1, 1\}^{M_d}. \tag{13}$$

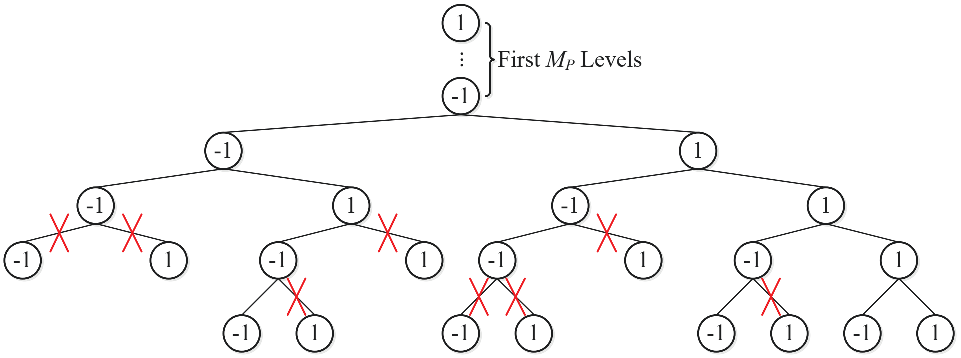

Fig. 2. Pruned tree search with at most 4 survival candidates at each level.

In eq. (13), $\mathbf{x}_p$ contained in $\mathbf{x}$ is known and fixed as pilots, and we only optimize the objective function with respect to $\mathbf{x}_d$. In general, if $\mathbf{x}$ is the ground truth, $\mathbf{Yx}$ can be a good approximation to $\mathbf{h}$, because $\mathbf{Yx} = \mathbf{C}_{\mathbf{x}}^T\mathbf{C}_{\mathbf{x}}\mathbf{h} + \mathbf{C}_{\mathbf{x}}^T\mathbf{n}$ can be viewed as part of the signal $\mathbf{h} * \text{Auto}(\mathbf{x})$ plus noise, where $\text{Auto}(\mathbf{x})$ refers to as the auto-correlation of signal $\mathbf{x}$. Since elements of $\mathbf{x}$ can be viewed as independent random variable in equalizer (without the knowledge of channel encoder), the $\text{Auto}(\mathbf{x})$ can be spiky, and $\mathbf{h} * \text{Auto}(\mathbf{x})$ preserves the sparsity of $\mathbf{h}$. l_4-norm is used here to encourage sparsity and it is not sensitive to noise compared with l_1-norm [11, 12]. The l_n-norm is defined as

$$||\mathbf{v}||_{l_n} = (\sum_i |v(i)|^n)^{1/n} \tag{14}$$

where $\mathbf{v}$ is a complex vector.

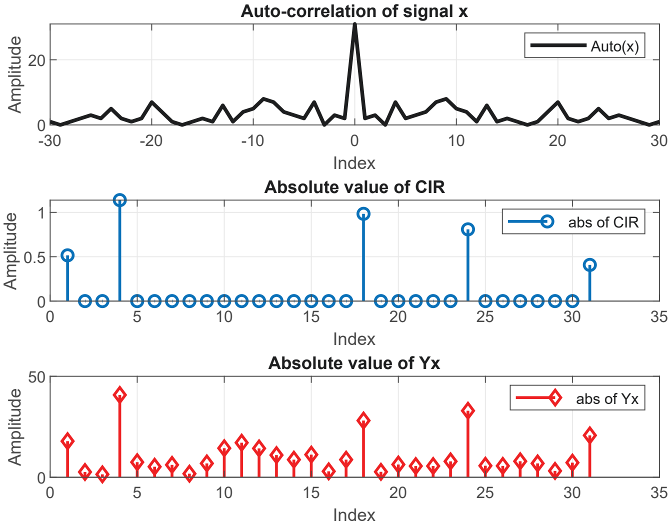

Fig. 3. Example of $\mathbf{Yx}$ preserving sparsity of $\mathbf{h}$.

Fig. 3 shows an example of $\text{Auto}(\mathbf{x})$, $||\mathbf{h}||_{l_2}$ and $||\mathbf{Yx}||_{l_2}$. The black solid curve refers to as the auto-correlation of a 31-bits long BPSK signal $\mathbf{x}$, which is spiky as we expected. The blue circle stem shows the absolute value of CIR of a 31-bits long sparse channel $\mathbf{h}$. The red diamond stem shows the absolute value of signal $\mathbf{Yx}$. If we viewed non-zero entries with small values as noise in the bottom subfigure, sparsity of $\mathbf{h}$ is preserved.

The feasible set $\{-1,1\}^{M_d}$ is discrete and non-convex, so we relax it to its convex-hull $[-1,1]^{M_d}$ and form problem

$$\begin{aligned} \min_{\mathbf{x}=[\mathbf{x}_p,\mathbf{x}_d]} \; & -\frac{1}{4}||\mathbf{Yx}||_{l_4}^4 \\ s.t. \;\; & \mathbf{x}_d \in [-1,1]^{M_d}. \end{aligned} \tag{15}$$

Note that problems in eq. (13) and eq. (15) yield same solution, because the objective function is strongly concave almost everywhere, and local minimizers of a strongly concave function over a closed convex set must be extreme points of the set, and the set $\{-1,1\}^{M_d}$ consists of all extreme points of $[-1,1]^{M_d}$. Successive underestimation methods (SUM) are often used to deal with concave minimization over convex sets [13], however it involves vertices enumeration of polyhedral sets. When a problem has relative large size, the computational complexity of SUM becomes prohibitive. Therefore, gradient descent methods are used here to find an optimal solution.

C. Initialization

An initialization close to ground truth makes gradient-based algorithms more likely to converge to global minimum. Here a pruned tree search algorithm [14–16] is proposed for initialization. Denote $\mathbf{y}_k$, $\mathbf{h}_k$ with definition in Section II, and

$$\mathbf{X}_k = \begin{bmatrix} x(1) & & & \\ x(2) & x(1) & & \\ \vdots & \vdots & \ddots & \\ x(k) & x(k-1) & \dots & x(1) \end{bmatrix} \tag{16}$$

we define the k-th subproblem in initialization as

$$\begin{aligned} \min_{\mathbf{x}_d \in \mathbb{R}, \mathbf{h}_k \in \mathbb{C}^{k \times 1}} \; & ||\mathbf{y}_k - \mathbf{X}_k\mathbf{h}_k||_{l_2}^2 + \lambda\rho(\mathbf{h}_k) \\ s.t. \;\; & \mathbf{x}_d \in \{-1,1\}^{M_d} \end{aligned} \tag{17}$$

where $\rho(\mathbf{h}_k)$ is the penalty, which is necessary here, otherwise one can easily find pairs of $\mathbf{x}_d$ and $\mathbf{h}_M$ such that $||\mathbf{y}_k - \mathbf{X}_k\mathbf{h}_k||_{l_2} = 0$. We use the results of the M-th subproblem as the initialization of our main problem in eq. (15). The pruned tree search begins at the 1-st level and ends at the M-th level, which is the bottom of the tree. At the k-th level, each leaf node is extended into 2 new leaf nodes at $(k+1)$-th level. Then with a chosen metric, we keep at most T nodes at the $(k+1)$-th level, where T is a pre-selected value.

Basically, the larger the T, the better the error performance of the algorithm. If T is large enough such that no node is pruned, the algorithm is equivalent to exhaustive search. Fig. 2 gives an example of this process. In the figure, T is set to 4, so each level can preserve at most 4 survival leaf nodes. Before the (M_P+2)-th level (including M_P+2), all survival paths are preserved. At the (M_P+3)-th level, 8 nodes are extended from last level while only 4 can be preserved. The (M_P+4)-th level is in a similar process.

We use the following metric when pruning nodes. At the k-th level, consider a leaf node $x(k)$, and denote the path of it from the 1-st level to the k-th level as $[x(1), x(2), .., x(k)]^T$, then the metric is computed as $J_k(x(1), x(2), .., x(k)) = \min_{\mathbf{h}_k \in \mathbb{C}^{k\times 1}} ||\mathbf{y}_k - \mathbf{X}_k\mathbf{h}_k||_{l_2}^2 + \lambda\rho(\mathbf{h}_k)$. Note that we calculate J_k with the knowledge of $\mathbf{X}_k$, which is associated with the path to the node.

Since we have M_p pilots, from the 1-st to the M_p-th level, there is only one path $\mathbf{x}_p$. At the bottom level, the path with smallest metric J_M is taken as hard output, and the approximate log likelihood ratio (LLR) can be calculated as

$$\begin{aligned}\mathrm{LLR}(x_i) = & \min_{\mathbf{x}\in\mathbf{S}_i^{(-1)}} J_M(x(1), x(2), .., x(M))/\sigma^2 \\ & - \min_{\mathbf{x}\in\mathbf{S}_i^{(1)}} J_M(x(1), x(2), .., x(M))/\sigma^2\end{aligned} \tag{18}$$

where $\mathbf{S}_i^a$ refers to as the set of paths that survive at bottom level such that $x(i) = a$ [14], and the LLR format is given as $\mathrm{LLR}(x) = \log(\frac{\mathrm{p}(x=+1)}{\mathrm{p}(x=-1)})$. The following algorithm summarizes the pruned tree search process mentioned above.

Pruned Tree Search Algorithm

```
Initialize first $M_p$ levels of the tree.
for $k$ from $M_p + 1$ to $M$, do
    Extend the $k$-th level to have the $(k+1)$-th level node candidates.
    Preserve at most $T$ nodes at the $(k+1)$-th level with smallest $J_k$.
end for
Output the $\mathbf{x}$ with smallest $J_M$ as hard decision.
Output the soft decision according to eq. (18).
```

After this process, the mean value of each x_i can be calculated with $\mathrm{LLR}(x_i)$ as

$$\mathrm{E}\{x_i\} = \frac{\exp(\mathrm{LLR}(x_i)) - 1}{\exp(\mathrm{LLR}(x_i)) + 1} \tag{19}$$

and the value can be used as the initialization of problem eq. (15).

D. Algorithm Convergence Analysis

For simplicity, denote $\mathbf{Y}_p \in \mathbb{C}^{L\times M_p}$ as the first M_p columns of $\mathbf{Y}$ and $\mathbf{Y}_d \in \mathbb{C}^{L\times M_d}$ as the rest columns, so we have $\mathbf{Y} = [\mathbf{Y}_p, \mathbf{Y}_d]$. Then denote objective function $G(\mathbf{x}) = -\frac{1}{4}||\mathbf{Y}_p\mathbf{x}_p + \mathbf{Y}_d\mathbf{x}||_{l_4}^4$. Since $\mathbf{x}_p$ is known as pilots, $\mathbf{Y}_p\mathbf{x}_p$ is a constant vector. Before showing any theoretical results, we first make an assumption below.

Assumption 1. *Let $\mathbf{x}^*$ be a local minimizer of $G(\mathbf{x})$ on $K = [-1, 1]^{M_d}$, then $\forall i$, $\frac{\partial G(\mathbf{x}^*)}{\partial x^*(i)} \neq 0$.*

This assumption is quite reasonable. Because, if there exists i such that $\frac{\partial G(\mathbf{x})}{\partial x(i)}|_{\mathbf{x}=\mathbf{x}^*} = 0$, we can move the point $\mathbf{x}^*$ along the i-th axis a little bit to let the objective function decrease even though partial derivative along the i-th axis is 0, because objective function has negative curvature almost everywhere. Now we establish two lemmas and a theorem to describe the convergence properties of the problem.

Lemma 1. *Let $\mathbf{x}^*$ be a local minimizer of $G(\mathbf{x})$ on $K = [-1, 1]^{M_d}$. Define set*

$$S(\mathbf{x}^*) = \{\mathbf{z} \in K : \forall i, \frac{\partial G(\mathbf{z})}{\partial z(i)} x^*(i) < 0\} \tag{20}$$

then gradient descent algorithm can generate a sequence $\{\mathbf{d}_k\}_{k=0}^{\infty}$ that converge to $\mathbf{x}^*$, if the set

$$Q(\mathbf{d}_0, \mathbf{x}^*) = \{\mathbf{z} : \forall i, (z(i) - d_0(i))(z(i) - x^*(i)) \leq 0\} \tag{21}$$

is a subset of $S(\mathbf{x}^*)$, i.e. $Q(\mathbf{d}_0, \mathbf{x}^*) \subset S(\mathbf{x}^*)$, where $\mathbf{d}_0$ is the initial value.

Proof. See Appendix. ☐

Lemma 2. *Denote the $\mathbf{A} = \mathfrak{Re}(\mathbf{Y})$ and $\mathbf{B} = \mathfrak{Im}(\mathbf{Y})$, and define $\mathbf{A}_p$, $\mathbf{A}_d$, $\mathbf{B}_p$ and $\mathbf{B}_d$ in similar way defining $\mathbf{Y}_p$ and $\mathbf{Y}_d$. Further, we denote $\mathbf{a} = \mathbf{A}\mathbf{x}_p$, $\mathbf{b} = \mathbf{B}\mathbf{x}_p$, $\boldsymbol{\Psi}_a = \mathbf{a} + \mathbf{A}_d\mathbf{x}$, $\boldsymbol{\Psi}_b = \mathbf{b} + \mathbf{B}_d\mathbf{x}$, $\boldsymbol{\Xi}_a = [\mathbf{a}, \mathbf{A}_d]$ and $\boldsymbol{\Xi}_b = [\mathbf{b}, \mathbf{B}_d]$. For arbitrary $\mathbf{x}_1, \mathbf{x}_2 \in K$, where $K = [-1, 1]^{M_d}$ we have*

$$||\nabla G(\mathbf{x}_1) - \nabla G(\mathbf{x}_2)||_{l_2} \leq \gamma||\mathbf{x}_1 - \mathbf{x}_2||_{l_2} \tag{22}$$

where γ is given as

$$\begin{aligned}\gamma = & 3||\mathbf{A}_d||_2^2||\boldsymbol{\Xi}_a||_\infty^2 + 3||\mathbf{B}_d||_2^2||\boldsymbol{\Xi}_b||_\infty^2 \\ & + 4||\mathbf{A}_d||_2||\mathbf{B}_d||_2||\boldsymbol{\Xi}_a||_\infty||\boldsymbol{\Xi}_b||_\infty \\ & + ||\mathbf{A}_d||_2^2||\boldsymbol{\Xi}_b||_\infty^2 + ||\mathbf{B}_d||_2^2||\boldsymbol{\Xi}_a||_\infty^2.\end{aligned} \tag{23}$$

Proof. See Appendix. ☐

Theorem 1. *Let $\mathbf{x}^*$ be a local (global) minimizer of $G(x)$, then the gradient descent algorithm is guaranteed to generate a sequence $\{\mathbf{d}_k\}_{k=0}^{\infty}$ that converges to $\mathbf{x}^*$, if the initial point $\mathbf{d}_0$ satisfies*

$$||\mathbf{d}_0 - \mathbf{x}^*||_{l_2} < \frac{1}{\gamma}\min_i\{|\frac{\partial G(\mathbf{x}^*)}{\partial x^*(i)}|\} \tag{24}$$

where γ is defined in Lemma 2.

Proof. See Appendix. ☐

Theorem 1 generally states that all points in the ball centred at $\mathbf{x}^*$ with radius described in eq. (24) can be guaranteed to converge to $\mathbf{x}^*$.

E. Simulation Results and Analysis

In the simulation, we adopt the same parameters used in PNNL's fish-tag project for real-world IoT devices in underwater acoustic communication systems. An entire transmitted signal block has $M = 31$ bits, which include $M_p = 7$ bits barker code as pilots, $M_{d_1} = 16$ bits for the information data, and $M_{d_2} = 8$ bits as the cyclic redundancy check (CRC) bits. The block structure is shown in Fig. 4. At receiver end, a syndrome decoding is used after equalization to give final results.

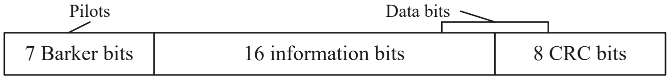

Fig. 4. Block structure used in the underwater animal tracking project.

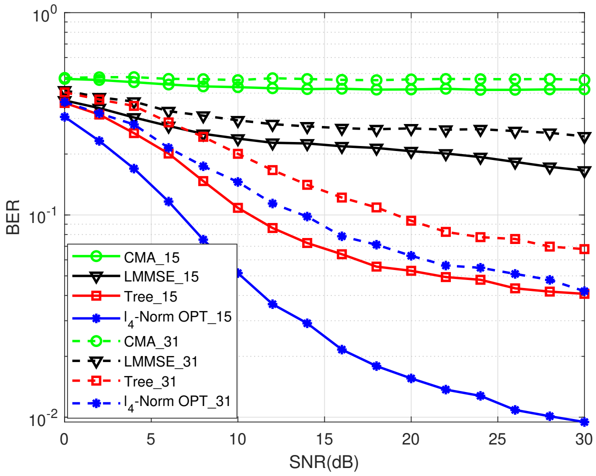

Fig. 5. BER comparison with length of CIRs being 15 and 31.

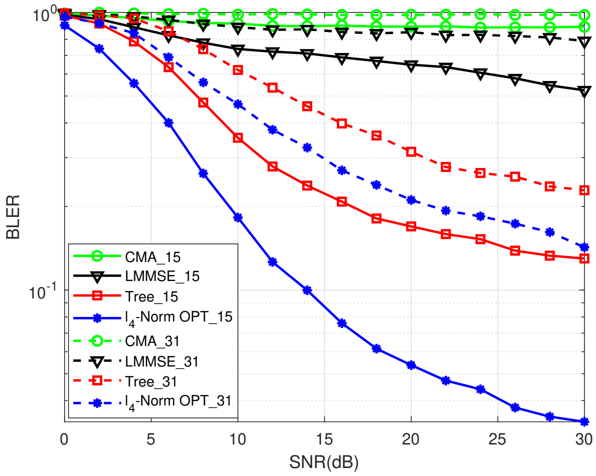

Fig. 6. BLER comparison with length of CIRs being 15 and 31.

Fig. 5 and Fig. 6 show bit error rate (BER) and block error rate (BLER) performance comparison among four algorithms followed by syndrome decoding: CMA, LMMSE, pruned tree search and l_4-norm optimization with pruned tree search initialization. In these two figures, the entries of channels are modeled as i.i.d. BG random variables with parameter as $\phi = 0.2$, i.e. for any k, the k-th entry of $\mathbf{h}$

$$h(k) = \varpi(k)\varrho(k) \tag{25}$$

where $\varpi(k) \sim \mathrm{Ber}(\phi)$ and $\varrho(k) \sim \mathcal{CN}(0, 1)$. Here $\mathrm{Ber}(\phi)$ refers to as Bernoulli distribution with $\Pr(\varpi(k) = 1) = \phi$. We model channel as eq. (25) because underwater channels are often sparse [17]. Apparently, the smaller the ϕ, the sparse the channel we modeled.

According to Fig. 5 and Fig. 6, we can see the CMA performs poorly in this parameter setting, because only a small number of bits are transmitted. The CMA basically adjusts the linear equalizer coefficients based on the error of estimated signal envelopes. If a large number of received symbols are given, the empirical loss calculated by these symbols can accurately approximate the true loss of CMA, which is the expected error of estimated signal envelops. Unfortunately, the received symbols are too few to support CMA. LMMSE also performs poorly, since it can only estimate first $M_p = 7$ taps of CIR according to eq. (6) [2].

The square-marked red curves are corresponding to the BER and BLER of pruned tree search initialization proposed in Section III-C. We choose $\rho(\mathbf{h}_k) = ||\mathbf{h}_k||_{l_2}^2$, simply because it yields explicit expression for J_k, i.e.

$$\begin{aligned} J_k &= \min_{\mathbf{h}_k \in \mathbb{C}^{k \times 1}} ||\mathbf{y}_k - \mathbf{X}_k \mathbf{h}_k||_{l_2}^2 + \lambda ||\mathbf{h}_k||_{l_2}^2 \\ &= \lambda \mathbf{y}_k^H (\mathbf{X}_k \mathbf{X}_k^H + \lambda \mathbf{I})^{-1} \mathbf{y}_k. \end{aligned} \tag{26}$$

As we can see, the pruned tree search performs much better than the other two. The star-marked blue curves show the performance of the proposed l_4-norm optimization with pruned tree search initialization, and its performance is better than the other three. Note that, to reduce computational complexity, we first check the hard output of tree search initialization. If it passes the CRC check, we directly output it as final result, otherwise we use estimated mean values given by eq. (19) to initialize the l_4-norm optimization to perform equalization and then decoding.

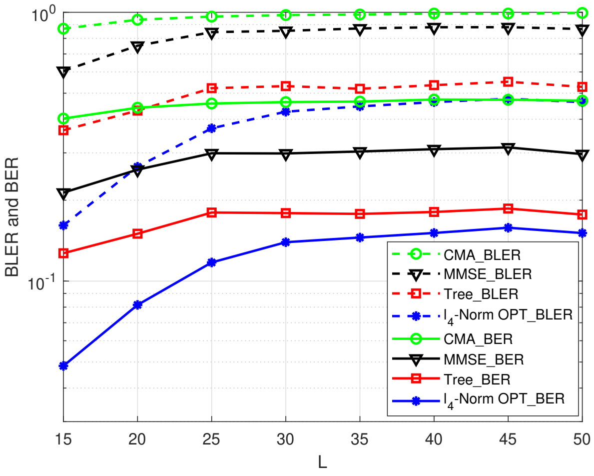

Fig. 7. BLER and BER with different L at SNR 30 dB.

---

[2] In conventional communication systems, M_p pilots can only estimate at most $(M_p + 1)/2$ taps of CIR with linear methods. However, in this system, they can estimate M_p taps with linear methods, since the head of received signal $\mathbf{y}$ is used. Note that, in eq. (6), $\mathbf{C}_{\mathbf{x}, M_p}$ is a lower triangular matrix which contains only pilots.

In simulations, signal-to-noise ratio (SNR) is defined as

$$\mathrm{SNR} = 10\log_{10}\frac{||\mathbf{h}||_{l_2}^2}{\sigma^2}. \tag{27}$$

At the same SNR, algorithms perform better when length of CIRs are shorter, because inter-symbol-interference (ISI) is weaker. Without surprise, simulation results in Fig. 7 show lower BLER and BER with short CIRs.

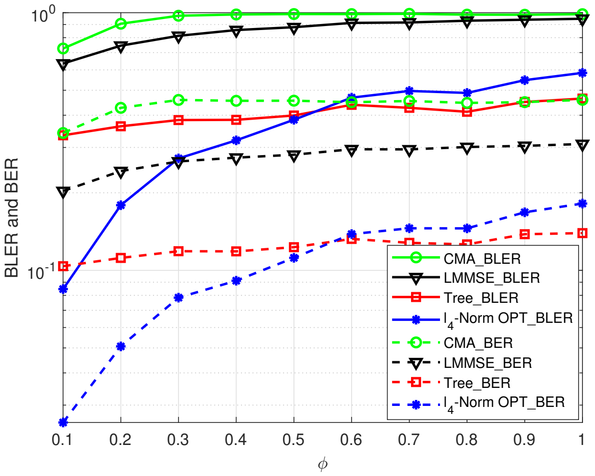

Fig. 8. BLER and BER under different ϕ with length-15 CIR at SNR 10 dB.

Fig. 8 shows the change of error performances with respect to different value of sparse parameter ϕ. In the simulation, the length of CIR is chosen as 15 and SNR is set as 10 dB. According to Fig. 8, the pruned tree search initialized l_4-norm optimization performs much better with smaller ϕ, which means the channel is sparse. When ϕ grows larger, its performance gradually degraded.

IV. DATA PROCESSING AND RESULTS

The real-world data are from an underwater animal tracking project developed by PNNL. In this project, carrier frequency is $f_c = 416.667$ kHz, sample frequency is $f_s = 2.5$ MHz, so the sample duration is $T_s = 1/f_s = 0.4$ μs, and bit duration is $T_b = N_sT_s$, where $N_s = 60$ refers to as the number of samples for each data bit. Each transmission block contains $M_p = 7$ bits barker code as pilots, $M_d = 24$ data bits. Among the $M_d = 24$ data bits, $M_{d_1} = 16$ are information bits, and the rest $M_{d_2} = 8$ bits are CRC bits.

The pulse shaping filter is given as [3]

$$p(t) = \begin{cases} 1, & 0 < t \leq T_b \\ 0, & otherwise. \end{cases} \tag{28}$$

Each recording contains $N_t = 40,960$ samples, equally $16,400$ μs, and signals may appear anywhere in the recording.

A. Block Synchronization

In each recording, we need to know when the desired signal begins. The desired signals are not necessary to appear at any fixed time or sample indexes, so block synchronization is necessary after coherent demodulation (i.e. remove carrier frequency).

Due to the fact that pilots are short, CIRs are long and sparse, conventional block synchronization does not work properly, therefore we propose a new method to perform block synchronization [18, 19].

Denote the baseband barker signal as

$$b_{barker}(t) = \sum_{i=1}^{M_p} x_p(i)p(t-(i-1)T_b) \tag{29}$$

and the T_s sampled baseband barker signal as vector $\mathbf{b}_{barker} \in \mathbb{R}^{M_pN_s\times 1}$. Let $\tilde{\mathbf{y}} \in \mathbb{C}^{N_t\times 1}$ denote the recording after coherent demodulation, which is T_s sampled. Then for an index i to be the starting position, it must satisfy following two conditions. First, a shape condition is given by

$$\frac{||\mathbf{b}_{barker}^H\tilde{\mathbf{y}}(i:i+M_pN_s-1)||_{l_2}}{||\mathbf{b}_{barker}||_{l_2}||\tilde{\mathbf{y}}(i:i+M_pN_s-1)||_{l_2}} > \eta_1 \tag{30}$$

where η_1 is a chosen parameter. Note that energy is normalized for $\tilde{\mathbf{y}}(i : i+M_pN_s-1)$ instead of $\tilde{\mathbf{y}}$, so only shapes of the signals are considered. Indexes satisfying this condition turn out to be consecutive groups, for example $[\{1,2,3\},\{8,9,10,11,12\},\{40\}]$. We choose the index at center of each group as candidates which are $[\{2\},\{10\},\{40\}]$, since they are often the ones with highest correlation values in its group. Second, an energy condition is given by

$$\frac{1}{MN_s}||\tilde{\mathbf{y}}(i:i+MN_s-1)||_{l_2} > \eta_2\frac{1}{N_t}||\tilde{\mathbf{y}}||_{l_2}. \tag{31}$$

This means that energy of length-MN_s signals starting from i should be higher than a chosen threshold η_2 times the average energy of the recording. With these two conditions, we can narrow down starting positions of signal to a few possible candidates.

B. Frequency Shift Error and Initial Phase Estimation

In this subsection, we use received pilot signals, i.e. $\tilde{\mathbf{y}}(i : i+M_pN_s-1)$ where i is a starting position of transmitted signals, to estimate frequency shift Δf and θ. We consider the case that pilots are much shorter than the delay of channel, so we assume that no echo begins during pilots. Denote $\mathbf{y}_{barker}$ as the vector generated by downsampling $\tilde{\mathbf{y}}(i:i+M_pN_s-1)$ by N_s, then we have symbol-spaced received pilot signal,

$$\mathbf{y}_{barker}(n) = A\mathbf{x}_p(n)e^{j(2\pi\Delta f(n-1)T_b-\theta)} + \mathbf{w}(n) \tag{32}$$

where $\mathbf{w}(n)$ is the noise and $A > 0$ is the amplitude of channel's first tap. Consider the phase difference between $\mathbf{y}_{barker}$ with $\mathbf{x}_p$, we have

$$\angle\frac{\mathbf{y}_{barker}(n)}{\mathbf{x}_p(n)} = 2\pi\Delta f(n-1)T_b - \theta + \angle\mathbf{w}. \tag{33}$$

---

[3] The original IoT devices and signals were designed with limited energy constraints and complexity which are not necessarily optimal in terms of conventional communication pulse shaping.

Denote $\Delta\angle \mathbf{x}_p(n) = \angle \frac{\mathbf{y}_{barker}(n)}{\mathbf{x}_p(n)}$, and

$$\mathbf{U} = \begin{bmatrix} 0 & -1 \\ 2\pi T_b & -1 \\ \vdots & \vdots \\ 2\pi(n-1)T_b & -1 \end{bmatrix}. \tag{34}$$

Write eq. (33) in matrix form, we have

$$\Delta\angle \mathbf{x}_p = \mathbf{U} \begin{bmatrix} \Delta f \\ \theta \end{bmatrix} + \angle \mathbf{w}. \tag{35}$$

With zero-forcing (ZF), we estimate Δf and θ as

$$\begin{bmatrix} \Delta f \\ \theta \end{bmatrix} = (\mathbf{U}^T\mathbf{U})^{-1}\mathbf{U}^T \Delta\angle \mathbf{x}_p(n). \tag{36}$$

After compensate the frequency shift error and initial phase, the sampled signal $\mathbf{y}$ is used for equalization and decoding.

C. Equalization and Decoding

In this project, we assume maximum length of the CIR as $L = 31$. We roughly estimate noise variance σ^2 by calculating the average energy of samples before the first start position.

Before equalization and decoding, we first make a hard decision on $\mathbf{y}$ to have $\hat{\mathbf{x}}$. Then we check if $\hat{\mathbf{x}}$ passes the CRC and the correlation between signal $\mathbf{b}_{\hat{\mathbf{x}}}$ and MN_s samples of $\tilde{\mathbf{y}}$ after start position i being larger than a threshold η_3, i.e.

$$\frac{||\mathbf{b}_{\hat{\mathbf{x}}}{}^H \tilde{\mathbf{y}}(i : i + MN_s - 1)||_{l_2}}{||\mathbf{b}_{\hat{\mathbf{x}}}||_{l_2} ||\tilde{\mathbf{y}}(i : i + MN_s - 1)||_{l_2}} > \eta_3 \tag{37}$$

where $\mathbf{b}_{\hat{\mathbf{x}}}$ is given by

$$b_{\hat{\mathbf{x}}}(n) = \sum_{i=1}^{M} \hat{x}(i) p(nT_s - (i-1)N_s T_s). \tag{38}$$

If both conditions are satisfied, we directly output $\hat{\mathbf{x}}$ as the final result, otherwise we perform equalization and decoding mentioned in Section III-E to give final results.

D. Data Processing Results

To demonstrate the efficacy of our new algorithm, two groups (G1, G2) of IoT data were processed by the following five algorithms: 1) raw detection (no equalization or decoding); 2) syndrome decoding only; 3) CMA equalization and syndrome decoding; 4) LMMSE equalization and syndrome decoding; and 5) our proposed new equalization and syndrome decoding. Each group of the data contains 14,000 recordings.

The successful detection rates of these five algorithms are listed in Table I, which can draw three clear observations: a) the syndrome decoding algorithm provides better results than raw detection, which has no surprise; b) CMA equalization plus syndrome decoding and LMMSE equalization plus syndrome decoding lead to degraded performance compared to syndrome decoding only, since signals output from CMA and LMMSE equalizers are far from the ground-truth such that the number of errors is larger than correction capability of the channel codes; c) our new equalization and syndrome decoding algorithm provides significantly improved performance compared to syndrome decoding only.

TABLE I
COMPARISON OF SUCCESSFUL DETECTION RATE.

Items	**G1**	**G2**
Raw Detection	13.64%	48.01%
Decoding-Only	21.94%	55.98%
CMA and Decoding	16.47%	49.81%
LMMSE and Decoding	20.21%	51.53%
New Equalization and Decoding	31.31%	66.07%

E. Example A

Fig. 9 gives an example of intermediate results for processing a data recording. The top subfigure in Fig. 9 shows the absolute value of the baseband recording. The middle subfigure gives correlation between the baseband recording and barker code signal according to left hand side of eq. (30). After check the energy condition according to eq. (31), the algorithm gives 4 possible starting positions as $\{11513, 12102, 12696, 13489\}$. We takes the first one (11513) as an example, which is highlighted by a red circle. As we can see it is a very high peak of correlation which means the baseband signal start there looks similar to barker code signal. The noise power σ^2 was estimated by samples between positions 0 and 11513.

Then frequency shift error and initial phase are estimated and compensated according to Section IV-B. The Doppler shift is estimated as 193 Hz. After that the signal in the red block in top subfigure is shown in the bottom subfigure, which has 31 bits duration. In the subfigure we can clearly recognize the 7 bits barker code and some bits following them. However, the amplitude of signal changes a lot after the 8-th bit, and the shape of signal for each bit looks very much different from rectangular pulse shaping filter used in this project. Apparently, some echoes come in after the 8-th bit.

Then the signal in bottom subfigure and following $L - 1 = 30$ bits signal after it are downsampled to get $\mathbf{y}$. After that, the algorithm first check if the first 31 entries of $\mathbf{y}$ (the hard decision in bottom subfigure) pass CRC and it turns out to be not. Then proposed equalization and decoding is applied to give final results.

Fig. 10 gives the estimated CIR with the final decoding results. Strong echo peaks appear at $\{9, 11, 19\}$-th bit positions, which is compatible with the observation in bottom subfigure.

F. Example B

The Fig. 11 gives another recording example. Apparently, the signal is very clean at beginning, and the block synchronization finds the starting position of signal accurately. The Doppler is estimated as 80 Hz. However, some echoes come in at the 10-th symbol position, which makes signal after the 10-th symbol awkward. Then we use the proposed methods to process the signal, and finally get decoded signal pass CRC. The CIR inferred from decoded symbols is given in Fig. 12.

It is important to point out that the CIR of examples A and B are longer than the pilot length, conventional channel estimation approaches are not able to estimate the channel, therefore reliable data detection becomes impossible by conventional communication algorithms. Furthermore, due to the

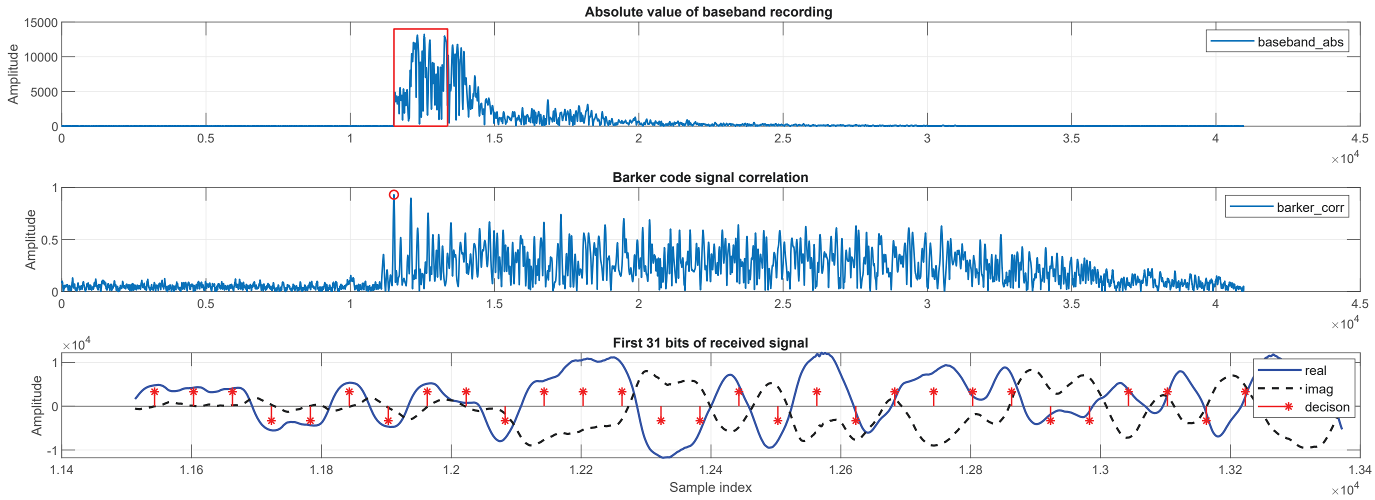

Fig. 9. Example of recording (A). Absolute value of baseband recording, barker code signal correlation and first 31 bits of received signal are contained.

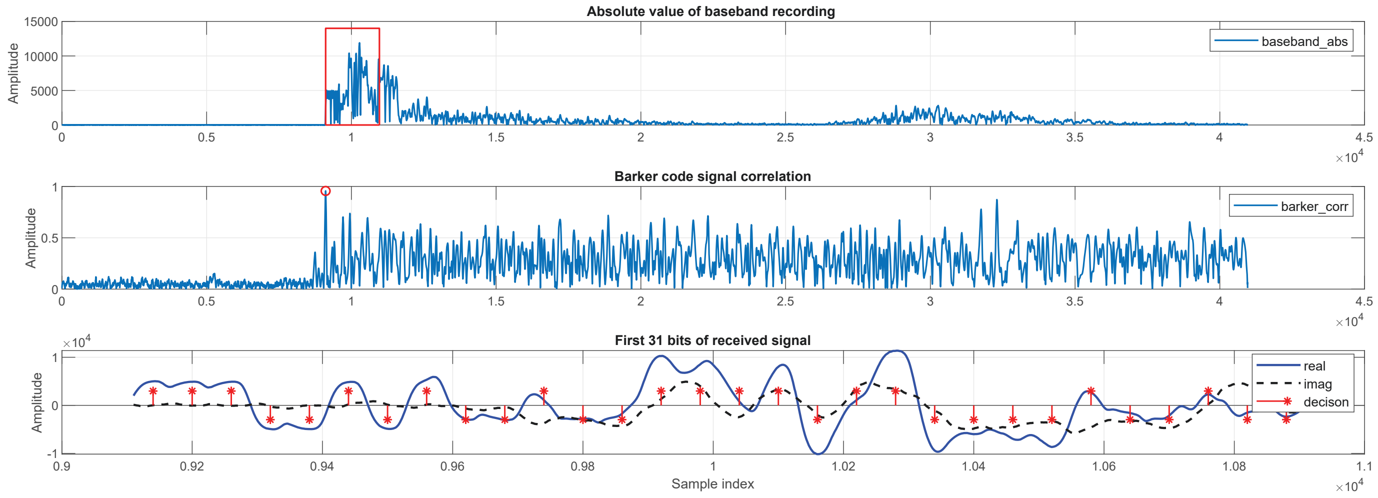

Fig. 11. Example of recording (B). Absolute value of baseband recording, barker code signal correlation and first 31 bits of received signal are contained.

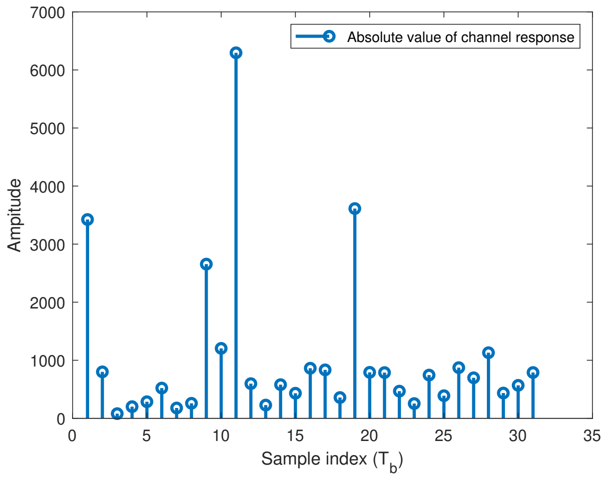

Fig. 10. Absolute value of CIR in example A.

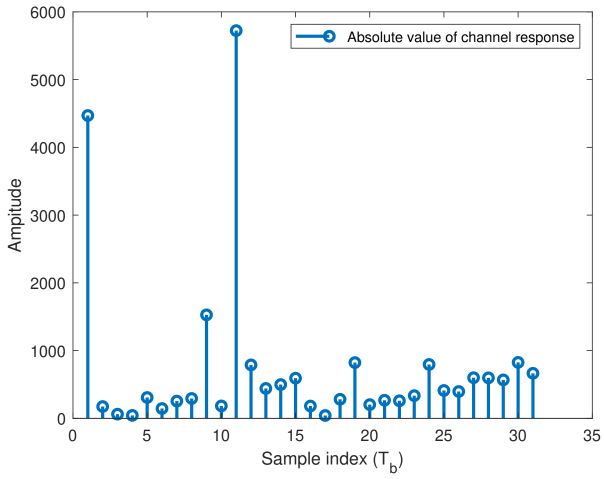

Fig. 12. Absolute value of CIR in example B.

short length of signals, blind equalization is not possible either to detect the information data.

V. CONCLUSION

We considered the scenario of short message transmission with IoT devices in underwater acoustic communication, where the length of pilots is shorter than the channel impulse response. This makes conventional channel estimation and equalization incapable of detecting the information data. In this paper, we proposed a novel channel equalization and decoding algorithm to combat severe frequency selective channels. Inspired by strategies in blind deconvolution and compressive sensing, we constructed a non-convex optimization problem and developed a method to find good initialization. By solving the non-convex optimization problem we made very good detection on signals. In additional, a complete procedure of real-world data processing are illustrated in this paper, including block synchronization, frequency shift error estimation, and proposed equalization and decoding methods. Our proposed new algorithm was utilized to process $28,000$ fish-tag data recordings, the results showed that our proposed algorithm provides significant advantage on data detection performance.

APPENDIX A
PROOF OF THEOREM 1

A. Proof for Lemma 1

Proof. Suppose $\mathbf{d}_k \in S(\mathbf{x}^*)$ at the k-th iteration, then at $(k+1)$-th iteration, gradient descent gives

$$\mathbf{d}_{k+1} = \mathbf{d}_k - \alpha_k \nabla G(\mathbf{d}_k) \odot \nu_k \tag{39}$$

where $\odot$ refers to as element wise multiplication, α_k is step-size such that $\mathbf{d}_{k+1}$ will not exceed boundary (α_k is usually chosen as a constant. If $\mathbf{d}_{k+1}$ exceeds the boundary, then choose α_k such that $\mathbf{d}_{k+1}$ is on the boundary), and ν_k is a vector indicating whether the corresponding boundaries are active. The i-th entry of ν_k is 0 if $d_k(i) \in \{-1, 1\}$, and is 1 if $d_k(i) \notin \{-1, 1\}$.

Since $\mathbf{d}_k \in S(\mathbf{x}^*)$, we have

$$x^*(i) d_k(i) \leq x^*(i) d_{k+1}(i) \leq 1. \tag{40}$$

This implies that for all i, there exists $\beta_i \in [0, 1]$ such that

$$x^*(i) d_{k+1}(i) = \beta_i x^*(i) d_k(i) + (1 - \beta_i). \tag{41}$$

Multiply $x^*(i)$ with both sides of eq. (41) and note the fact $x^*(i)^2 = 1$, we have

$$d_{k+1}(i) = \beta_i d_k(i) + x^*(i)(1 - \beta_i) \tag{42}$$

which implies that $\mathbf{d}_{k+1} \in Q(\mathbf{d}_k, \mathbf{x}^*)$. Therefore

$$\mathbf{d}_{k+1} \in Q(\mathbf{d}_{k+1}, \mathbf{x}^*) \subseteq Q(\mathbf{d}_k, \mathbf{x}^*) \subseteq \ldots \subseteq Q(\mathbf{d}_0, \mathbf{x}^*). \tag{43}$$

So far we have proved that $\{\mathbf{d}_k\}_{k=0}^{\infty}$ are bounded. Then we consider the sequence $\{x^*(i) d_k(i)\}_{k=0}^{\infty}$. The sequence $\{x^*(i) d_k(i)\}_{k=0}^{\infty}$ is bounded since $\{\mathbf{d}_k\}_{k=0}^{\infty}$ is bounded, and it is non-decreasing according to eq. (40). Therefore $\{x^*(i) d_k(i)\}_{k=0}^{\infty}$ converges. Since $Q(\mathbf{d}_0, \mathbf{x}^*)$ is closed and bounded, $x^*(i) \frac{\partial G(\mathbf{d}_k)}{\partial d_k(i)}$ has minimum larger than 0 for all i. Therefore the only way to make $\{x^*(i) d_k(i)\}_{k=0}^{\infty}$ converge is $\nu_k(i) = 0$, which means all boundaries are active, so $\{\mathbf{d}_k(i)\}_{k=0}^{\infty}$ converges to $\mathbf{x}^*$.

$\square$

B. Proof for Lemma 2

Proof. With previous definition, the objective function $G(\mathbf{x})$ can be written as

$$G(\mathbf{x}) = -\frac{1}{4} ||\mathbf{\Psi}_a^{\odot 2} + \mathbf{\Psi}_b^{\odot 2}||_{l_2}^2 \tag{44}$$

where $(.)^{\odot 2}$ refers to as element wise square. The Hessian matrix of $G(\mathbf{x})$ is give by eq. (45). Denote spectral norm of a matrix as $||.||_2$, then we have an upper bound of $||\nabla^2 G(\mathbf{x})||_2$ given by eq. (46). In the derivation of eq. (46), we use the fact that for any matrix $\mathbf{P}$ and $\mathbf{Q}$

$$||\mathbf{P} + \mathbf{Q}||_2 \leq ||\mathbf{P}||_2 + ||\mathbf{Q}||_2 \tag{48}$$

$$||\mathbf{P}\mathbf{Q}||_2 \leq ||\mathbf{P}||_2 ||\mathbf{Q}||_2. \tag{49}$$

Note that

$$||\mathrm{diag}(\mathbf{\Psi}_a)||_2 \leq ||\mathbf{\Xi}_a||_{\infty} \tag{50}$$

$$||\mathrm{diag}(\mathbf{\Psi}_b)||_2 \leq ||\mathbf{\Xi}_b||_{\infty} \tag{51}$$

where $||.||_{\infty}$ is defined as

$$||\mathbf{P}||_{\infty} = \max_i \Big(\sum_j |P(i, j)|\Big). \tag{52}$$

The reason why eq. (50) and eq. (51) hold is that $\mathbf{x} \in [-1, 1]^{M_d}$. Then from eq. (46), we can further have eq. (47) by eq. (50) and eq. (51). Denote γ as the right hand side of eq. (47). Then by mean value theorem, for any $\mathbf{x}_1$ and $\mathbf{x}_2$, there exists $\beta \in [0, 1]$ and $\bar{\mathbf{x}} = \beta \mathbf{x}_1 + (1 - \beta)\mathbf{x}_2$ such that

$$\nabla G(\mathbf{x}_1) - \nabla G(\mathbf{x}_2) = \nabla^2 G(\bar{\mathbf{x}})(\mathbf{x}_1 - \mathbf{x}_2). \tag{53}$$

Therefore we have

$$\begin{aligned} ||\nabla G(\mathbf{x}_1) - \nabla G(\mathbf{x}_2)||_{l_2} &\leq ||\nabla^2 G(\bar{\mathbf{x}})||_2 ||\mathbf{x}_1 - \mathbf{x}_2||_{l_2} \\ &\leq \gamma ||\mathbf{x}_1 - \mathbf{x}_2||_{l_2}. \end{aligned} \tag{54}$$

$\square$

C. Proof for Theorem 1

Proof. For any $\mathbf{d}_0$ such that eq. (24) holds, we have

$$||\nabla G(\mathbf{d}_0) - \nabla G(\mathbf{x}^*)||_{l_2} \leq \gamma ||\mathbf{d}_0 - \mathbf{x}^*||_{l_2} < \min_i \{|\frac{\partial G(\mathbf{x}^*)}{\partial x^*(i)}|\} \tag{55}$$

where first inequality is due to Lemma 2. Therefore we have

$$\forall i, \frac{\partial G(\mathbf{x}^*)}{\partial x^*(i)} \frac{\partial G(\mathbf{d}_0)}{\partial d_0(i)} > 0. \tag{56}$$

Since $\mathbf{x}^*$ is a local minimizer, with Karush-Kuhn-Tucker (KKT) conditions satisfied, we have

$$\forall i, \frac{\partial G(\mathbf{x}^*)}{\partial x^*(i)} x^*(i) < 0. \tag{57}$$

$$\begin{aligned}\nabla^2 G(\mathbf{x}) =& -[2(\mathbf{A}_d^T \mathrm{diag}(\mathbf{\Psi}_a) + \mathbf{B}_d^T \mathrm{diag}(\mathbf{\Psi}_b))(\mathbf{A}_d^T \mathrm{diag}(\mathbf{\Psi}_a) + \mathbf{B}_d^T \mathrm{diag}(\mathbf{\Psi}_b))^T \\ &+ \mathbf{A}_d^T \mathrm{diag}(\mathbf{\Psi}_a^{\odot 2})\mathbf{A}_d + \mathbf{A}_d^T \mathrm{diag}(\mathbf{\Psi}_b^{\odot 2})\mathbf{A}_d + \mathbf{B}_d^T \mathrm{diag}(\mathbf{\Psi}_a^{\odot 2})\mathbf{B}_d + \mathbf{B}_d^T \mathrm{diag}(\mathbf{\Psi}_b^{\odot 2})\mathbf{B}_d]\end{aligned} \tag{45}$$

$$\begin{aligned}||\nabla^2 G(\mathbf{x})||_2 \le& ||2(\mathbf{A}_d^T \mathrm{diag}(\mathbf{\Psi}_a) + \mathbf{B}_d^T \mathrm{diag}(\mathbf{\Psi}_b))(\mathbf{A}_d^T \mathrm{diag}(\mathbf{\Psi}_a) + \mathbf{B}_d^T \mathrm{diag}(\mathbf{\Psi}_b))^T||_2 \\ &+ ||\mathbf{A}_d^T \mathrm{diag}(\mathbf{\Psi}_a^{\odot 2})\mathbf{A}_d||_2 + ||\mathbf{A}_d^T \mathrm{diag}(\mathbf{\Psi}_b^{\odot 2})\mathbf{A}_d||_2 + ||\mathbf{B}_d^T \mathrm{diag}(\mathbf{\Psi}_a^{\odot 2})\mathbf{B}_d||_2 + ||\mathbf{B}_d^T \mathrm{diag}(\mathbf{\Psi}_b^{\odot 2})\mathbf{B}_d||_2 \\ =& 2||\mathbf{A}_d^T \mathrm{diag}(\mathbf{\Psi}_a) + \mathbf{B}_d^T \mathrm{diag}(\mathbf{\Psi}_b)||_2^2 \\ &+ ||\mathbf{A}_d^T \mathrm{diag}(\mathbf{\Psi}_a)||_2^2 + ||\mathbf{A}_d^T \mathrm{diag}(\mathbf{\Psi}_b)||_2^2 + ||\mathbf{B}_d^T \mathrm{diag}(\mathbf{\Psi}_a)||_2^2 + ||\mathbf{B}_d^T \mathrm{diag}(\mathbf{\Psi}_b)||_2^2 \\ \le& 2(||\mathbf{A}_d^T \mathrm{diag}(\mathbf{\Psi}_a)||_2 + ||\mathbf{B}_d^T \mathrm{diag}(\mathbf{\Psi}_b)||_2)^2 \\ &+ ||\mathbf{A}_d^T \mathrm{diag}(\mathbf{\Psi}_a)||_2^2 + ||\mathbf{A}_d^T \mathrm{diag}(\mathbf{\Psi}_b)||_2^2 + ||\mathbf{B}_d^T \mathrm{diag}(\mathbf{\Psi}_a)||_2^2 + ||\mathbf{B}_d^T \mathrm{diag}(\mathbf{\Psi}_b)||_2^2\end{aligned} \tag{46}$$

$$||\nabla^2 G(\mathbf{x})||_2 \le 3||\mathbf{A}_d||_2^2||\Xi_a||_\infty^2 + 3||\mathbf{B}_d||_2^2||\Xi_b||_\infty^2 + 4||\mathbf{A}_d||_2||\mathbf{B}_d||_2||\Xi_a||_\infty||\Xi_b||_\infty + ||\mathbf{A}_d||_2^2||\Xi_b||_\infty^2 + ||\mathbf{B}_d||_2^2||\Xi_a||_\infty^2 \tag{47}$$

Combine eq. (56) with eq. (57) we have

$$\forall i, \frac{\partial G(\mathbf{d}_0)}{\partial d_0(i)} x^*(i) < 0. \tag{58}$$

This implies that

$$\{\mathbf{d}_0 : ||\mathbf{d}_0 - \mathbf{x}^*||_{l_2} \le \frac{1}{\gamma} \min_i \{|\frac{\partial G(\mathbf{x}^*)}{\partial x^*(i)}|\}\} \subseteq S(\mathbf{x}^*). \tag{59}$$

For any point $\mathbf{z} \in Q(\mathbf{d}_0, \mathbf{x}^*)$ we have

$$\begin{aligned}&||\mathbf{d}_0 - \mathbf{x}^*||_{l_2}^2 - ||\mathbf{z} - \mathbf{x}^*||_{l_2}^2 \\ =& ||\mathbf{z} - \mathbf{d}_0||_{l_2}^2 - 2(\mathbf{z} - \mathbf{d}_0)^T(\mathbf{z} - \mathbf{x}^*) \ge 0.\end{aligned} \tag{60}$$

Therefore $||\mathbf{z} - \mathbf{x}^*||_{l_2} < \frac{1}{\gamma} \min_i \{|\frac{\partial G(\mathbf{x}^*)}{\partial x^*(i)}|\}$, so

$$Q(\mathbf{d}_0, \mathbf{x}^*) \subset \{\mathbf{d}_0 : ||\mathbf{d}_0 - \mathbf{x}^*||_{l_2} < \frac{1}{\gamma} \min_i \{|\frac{\partial G(\mathbf{x}^*)}{\partial x^*(i)}|\}\}. \tag{61}$$

By eq. (59), we have

$$Q(\mathbf{d}_0, \mathbf{x}^*) \subset S(\mathbf{x}^*) \tag{62}$$

and by Lemma 1, $\mathbf{d}_0$ is guaranteed to converge to $\mathbf{x}^*$. □

REFERENCES

[1] D. Evans, “The internet of things: How the next evolution of the internet is changing everything,” *CISCO White Paper*, April.

[2] A. Zanella, N. Bui, A. Castellani, L. Vangelista, and M. Zorzi, “Internet of things for smart cities,” *IEEE Internet Things J.*, vol. 1, no. 1, pp. 22–32, Feb 2014.

[3] M. R. Palattella, M. Dohler, A. Grieco, G. Rizzo, J. Torsner, T. Engel, and L. Ladid, “Internet of things in the 5G era: Enablers, architecture, and business models,” *IEEE J. Sel. Areas Commun.*, vol. 34, no. 3, pp. 510–527, March 2016.

[4] M. Wollschlaeger, T. Sauter, and J. Jasperneite, “The future of industrial communication: Automation networks in the era of the internet of things and industry 4.0,” *IEEE Ind. Electron. Mag.*, vol. 11, no. 1, pp. 17–27, March 2017.

[5] S. Ramnath, A. Javali, B. Narang, P. Mishra, and S. K. Routray, “Iot based localization and tracking,” in *Proc. Int. Conf. IoT and Application (ICIOT)*, May 2017, pp. 1–4.

[6] M. H. Berlian, T. E. R. Sahputra, B. J. W. Ardi, L. W. Dzatmika, A. R. A. Besari, R. W. Sudibyo, and S. Sukaridhoto, “Design and implementation of smart environment monitoring and analytics in real-time system framework based on internet of underwater things and big data,” in *Proc. Int. Electronics Symposium (IES)*, Sep. 2016, pp. 403–408.

[7] R. Johnson, P. Schniter, T. J. Endres, J. D. Behm, D. R. Brown, and R. A. Casas, “Blind equalization using the constant modulus criterion: a review,” *Proceedings of the IEEE*, vol. 86, no. 10, pp. 1927–1950, Oct 1998.

[8] A.-J. van der Veen and A. Paulraj, “An analytical constant modulus algorithm,” *IEEE Trans. Signal Process.*, vol. 44, no. 5, pp. 1136–1155, May 1996.

[9] A. Ahmed, B. Recht, and J. Romberg, “Blind deconvolution using convex programming,” *IEEE Trans. Inf. Theory*, vol. 60, no. 3, pp. 1711–1732, March 2014.

[10] H.-W. Kuo, Y. Lau, Y. Zhang, and J. Wright, “Geometry and symmetry in short-and-sparse deconvolution,” *arXiv preprint arXiv:1901.00256*, 2019.

[11] Y. Li and Y. Bresler, “Global geometry of multichannel sparse blind deconvolution on the sphere,” in *Advances in Neural Information Processing Systems*, 2018, pp. 1132–1143.

[12] K. Nose-Filho and J. M. T. Romano, “On l_p-norm sparse blind deconvolution,” in *Proc. Int. Workshop on Machine Learning for Signal Process. (MLSP)*, Sep. 2014, pp. 1–6.

[13] K. L. Hoffman, “A method for globally minimizing concave functions over convex sets,” *mathematical Programming*, vol. 20, no. 1, pp. 22–32, 1981.

[14] J. Yang, C. Zhang, W. Song, S. Xu, and X. You, “Joint detection and decoding for MIMO systems with polar codes,” in *Proc. Int. Symposium on Circuits and Systems (ISCAS)*, May 2016, pp. 161–164.

[15] C. Liao, J. Wang, and Y. Huang, “A 3.1 gb/s 8 × 8 sorting reduced k-best detector with lattice reduction and qr decomposition,” *IEEE Trans. Very Large Scale Integr. (VLSI) Syst.*, vol. 22, no. 12, pp. 2675–2688, Dec 2014.

[16] S. Han, T. Cui, and C. Tellambura, “Improved K-best sphere detection for uncoded and coded MIMO systems,” *IEEE Wireless Commun. Lett.*, vol. 1, no. 5, pp. 472–475, October 2012.

[17] M. Stojanovic and J. Preisig, “Underwater acoustic communication channels: Propagation models and statistical characterization,” *IEEE Commun. Mag.*, vol. 47, no. 1, pp. 84–89, January 2009.

[18] K. G. Kebkal, V. K. Kebkal, O. G. Kebkal, and R. Petroccia, “Underwater acoustic modems (s2cr series) for synchronization of underwater acoustic network clocks during payload data exchange,” *IEEE J. Ocean. Eng.*, vol. 41, no. 2, pp. 428–439, April 2016.

[19] Z. Gong, C. Li, and F. Jiang, “Auv-aided joint localization and time synchronization for underwater acoustic sensor networks,” *IEEE Signal Process. Lett.*, vol. 25, no. 4, pp. 477–481, April 2018.

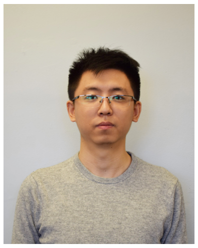

Shusen Jing (S'19) received B.E. degree in information science and engineering from Southeast University, Nanjing, China in 2017. He had 2017 outstanding bachelor thesis award of Southeast University. He had excellent paper award of 12th International Conference on ASIC (ASICON). He is currently a Ph.D. student in Lehigh University, Bethlehem, PA, USA. He mainly focuses on wireless communication and underwater acoustic communication.

Joseph received the Bachelor of Science in Electrical Engineering from Missouri University of Science and Technology in Rolla, MO in 2018. Joseph is currently a Computer Engineering Ph. D student at Lehigh University in Bethlehem, PA. His research focuses on embedded underwater communication systems. His research interests also include channel coding and FPGA-based physical layer acceleration for underwater acoustic communications. Joseph has also worked on acoustic telemetry systems for wildlife with Pacific Northwest National Laboratories in Richland, Washington.

Yahong Rosa Zheng (M'03-SM'07-F'15) received the B.S. degree from the University of Electronic Science and Technology of China, Chengdu, China, in 1987, and the M.S. degree from Tsinghua University, Beijing, China, in 1989. She received the Ph.D. degree from the Department of Systems and Computer Engineering, Carleton University, Ottawa, Canada, in 2002. She was an NSERC Postdoctoral Fellow from 2003 to 2005 at the University of Missouri-Columbia. From 2005–2018, she was with the Department of Electrical and Computer Engineering at the Missouri University of Science and Technology. She held the Wilkens' Missouri Telecommunications Endowed Professor position for 2017-2018 at Missouri S&T. She joined the ECE department at Lehigh University in Aug. 2018. Her research interests include underwater cyber-physical systems, real-time embedded systems, signal processing, wireless communications, and wireless sensor networks. She served as an Associate Editor for IEEE Transactions on Wireless Communications 2006-2008 and IEEE Transactions on Vehicular Technology 2008-2016. She has been Associate Editor for the IEEE Journal of Oceanic Engineering since 2016. She is the recipient of an NSF CAREER award in 2009. She has been a fellow of the IEEE and Distinguished Lecturer of IEEE Vehicular Technology Society since 2015.

Chengshan Xiao (M'99-SM'02-F'10) received a Bachelor of Science degree in electronic engineering from the University of Electronic Science and Technology of China in 1987, a Master of Science degree in electronic engineering from Tsinghua University in 1989, and a Ph.D. in electrical engineering from the University of Sydney in 1997. Dr. Xiao is the Chandler Weaver Professor and Chair of the Department of Electrical and Computer Engineering at Lehigh University. He is a Fellow of the IEEE and a Fellow of the Canadian Academy of Engineering. Previously, he served as a Program Director with the Division of Electrical, Communications and Cyber Systems at the USA National Science Foundation. He was a senior member of scientific staff with Nortel Networks, Ottawa, Canada, a faculty member at Tsinghua University, Beijing, China, the University of Alberta, Edmonton, Canada, the University of Missouri - Columbia, MO, and Missouri University of Science and Technology, Rolla, MO. He also held visiting professor positions in Germany and Hong Kong. His research interests include wireless communications, signal processing, and underwater acoustic communications. He is the holder of several patents granted in USA, Canada, China and Europe. His invented algorithms have been implemented into Nortel's base station radio products after successful technical field trials and network integration. Dr. Xiao is the Awards Committee Chair and elected Member-at-Large of Board of Governors of IEEE Communications Society. Previously, he served on the IEEE Technical Activity Board (TAB) Periodical Committee, he was an elected Member-at-Large of Board of Governors, a member of Fellow Evaluation Committee, Director of Conference Publications, Distinguished Lecturer of the IEEE Communications Society, and Distinguished Lecturer of the IEEE Vehicular Technology. He also served as an Editor, Area Editor and the Editor-in-Chief of the IEEE Transactions on Wireless Communications, an Associate Editor of the IEEE Transactions on Vehicular Technology, and of the IEEE Transactions on Circuits and Systems-I. He was the Technical Program Chair of the 2010 IEEE International Conference on Communications, Cape Town, South Africa, a Technical Program Co-Chair of the 2017 IEEE Global Communications Conference, Singapore. He served as the founding Chair of the IEEE Wireless Communications Technical Committee. He received several distinguished awards including 2014 Humboldt Research Award, 2014 IEEE Communications Society Joseph LoCicero Award, 2015 IEEE Wireless Communications Technical Committee Recognition Award, and 2017 IEEE Communications Society Harold Sobol Award.